



HAL
open science

Distribution of seismic scatterers in the San Jacinto Fault Zone, southeast of Anza, California, based on passive matrix imaging

Rita Touma, Alexandre Aubry, Yehuda Ben-Zion, Michel Campillo

► To cite this version:

Rita Touma, Alexandre Aubry, Yehuda Ben-Zion, Michel Campillo. Distribution of seismic scatterers in the San Jacinto Fault Zone, southeast of Anza, California, based on passive matrix imaging. *Earth and Planetary Science Letters*, 2022, 578, pp.117304. 10.1016/j.epsl.2021.117304 . hal-03262882v2

HAL Id: hal-03262882

<https://hal.science/hal-03262882v2>

Submitted on 10 Aug 2022

HAL is a multi-disciplinary open access archive for the deposit and dissemination of scientific research documents, whether they are published or not. The documents may come from teaching and research institutions in France or abroad, or from public or private research centers.

L'archive ouverte pluridisciplinaire **HAL**, est destinée au dépôt et à la diffusion de documents scientifiques de niveau recherche, publiés ou non, émanant des établissements d'enseignement et de recherche français ou étrangers, des laboratoires publics ou privés.

1 Highlights

2 **Distribution of seismic scatterers in the San Jacinto Fault Zone, southeast of** 3 **Anza, California, based on passive matrix imaging**

4 Rita Touma, Alexandre Aubry, Yehuda Ben-Zion, Michel Campillo

- 5 • A matrix approach allows resolving small-scale heterogeneities such as cracks
6 and fractures with an optimal resolution
- 7 • Scatterers and reflectors are imaged at the SGB site on the San Jacinto Fault
8 Zone, California
- 9 • Clear differences are found among different sections of the fault zone in the
10 study area

11 Distribution of seismic scatterers in the San Jacinto
12 Fault Zone, southeast of Anza, California, based on
13 passive matrix imaging

14 Rita Touma^{a,b}, Alexandre Aubry^b, Yehuda Ben-Zion^c, Michel Campillo^a

^aISTerre, Université Grenoble Alpes, Maison des Géosciences, BP 53, F-38041 Grenoble, France

^bInstitut Langevin, ESPCI Paris, PSL University, CNRS, 1 rue Jussieu, F-75005, Paris, France

*^cDepartment of Earth Sciences and Southern California Earthquake Center, University of
Southern California, Los Angeles, CA 90089, USA*

15 **Abstract**

Fault zones are associated with multi-scale heterogeneities of rock properties. Large scale variations may be imaged with conventional seismic reflection methods that detect offsets in geological units, and tomographic techniques that provide average seismic velocities in resolved volumes. However, characterizing elementary localized inhomogeneities of fault zones, such as cracks and fractures, constitutes a challenge for conventional techniques. Resolving these small-scale heterogeneities can provide detailed information for structural and mechanical models of fault zones. Recently, the reflection matrix approach utilizing body wave reflections in ambient noise cross-correlations was extended with the introduction of aberration corrections to handle the actual lateral velocity variations in the fault zone Touma et al. (2021). Here this method is applied further to analyze the distribution of scatterers in the first few kilometers of the crust in the San Jacinto Fault Zone at the Sage Brush Flat (SGB) site, southeast of Anza, California. The matrix approach allows us to image not only specular reflectors but also to resolve the presence, location and intensity of scatterers of seismic waves starting with

a simple homogeneous background velocity model of the medium. The derived three-dimensional image of the fault zone resolves lateral variations of scattering properties in the region within and around the surface fault traces, as well as differences between the Northwest (NW) and the Southeast (SE) parts of the study area. A localized intense damage zone at depth is observed in the SE section, suggesting that a geometrical complexity of the fault zone at depth induces ongoing generation of rock damage.

16 *Keywords:* Scattering, Fault zone structure, Passive imaging, Reflection matrix

17 **1. Introduction**

18 Earthquakes are among the most destructive natural disasters. Although earth-
19 quakes are generally unpredictable, some aspects of their behavior such as the
20 likelihood of being arrested and statistically-preferred propagation direction can
21 be estimated from structural properties of fault zones (see e.g. Chester et al.
22 (1993); Wesnousky (1988); Ben-Zion (2008)). Fault zones that are the structural
23 manifestation of earthquakes evolve during deformation and have generally com-
24 plex properties (e.g. Mitchell and Faulkner (2009); Ben-Zion and Sammis (2003)).
25 Characterizing the geometrical and seismic properties of fault zones can provide
26 important information for assessing likely past and future rupture properties. Fault
27 zones have also strong impact on fluid flow in the lithosphere (Knipe et al., 1998).

28 Fault zones are manifested at the surface by several main fault traces that
29 accommodate the bulk of the long term slip. They are characterized by linea-
30 ments, topography and various geometrical complexities. The identification of
31 fault traces is done by field observations (major line of fracturing, offset in ge-
32 ological units), along with remote sensing techniques that analyze ground de-

33 formation after major earthquakes obtained from satellites and aircrafts such as
34 Interferometric Synthetic Aperture Radar (InSAR, Massonnet et al. (1993)) and
35 subpixel correlation of optical images (SPOT, Binet and Bollinger (2005)). Fault
36 zone properties below the surface are obtained by seismic and other geophysical
37 imaging techniques.

38 Fault zones have hierarchical damage structures that evolve during the fault
39 zone activity and have several general elements (e.g. Chester et al. (1993); Rock-
40 well and Ben-Zion (2007)). The principle slip zone is a highly localized thin layer
41 (0.01 – 0.1 m thick) that accommodates most of the fault slip and is characterized
42 by ultra cataclasite rock particles. The principle slip zone is bounded by a core
43 damage zone (inner damage zone) that is typically about 100 m wide and asym-
44 metrically located on one side of the slip zone of large faults (Lewis et al., 2005;
45 Dor et al., 2006). The core damage is surrounded by a broader zone of reduced
46 damage intensity (referred to as outer damage zone) that may extend for several
47 km on each side of the fault. Properties of the fault zone damage provide infor-
48 mation on statistical tendencies of local earthquake ruptures, operating dynamic
49 stress field, energy dissipation and more (e.g. Manighetti et al. (2005); Mitchell
50 and Faulkner (2009); Xu et al. (2012)). For that reason, a number of seismic and
51 other methods have been developed to provide detailed information on fault zone
52 structures.

53 Among the seismic imaging techniques, reflection seismology is generally
54 pertinent to image planar horizontal layers with a very high resolution, and pro-
55 vide indirect imaging of faults by the offset of sedimentary layers. It relies on the
56 analysis of seismic waves that are sent back towards the surface after being re-
57 flected or scattered by subsurface structures with strong impedance contrasts. The

58 recorded wavefield is composed of reflected waves that result from the interaction
59 of seismic waves with planar reflectors such as layer boundaries, and diffracted
60 waves from small-scale geological objects such as cracks and fractures. To obtain
61 structural information on the subsurface, migration techniques are applied aiming
62 mainly to relocate reflectors and scatterers in depth or in time (see, e.g., review by
63 Etgen et al., 2009). Migration of seismic wavefields requires an accurate velocity
64 model of the Earth. Errors and biases in the velocity model produce artefacts and
65 defocusing due to phase distortions in the migrated images (Moser and Howard,
66 2008).

67 Reflection information is often gathered from seismic surveys where seis-
68 mic energy propagating into the medium is generated by man-made sources such
69 as vibrators, explosives, etc. In the last decade or so, passive methods based
70 on the ambient seismic noise have been developed to substitute active imaging
71 techniques (e.g. Campillo and Roux, 2014). Cross-correlation of passive traces
72 recorded at two receivers allows retrieving the Green's function between these
73 two receivers. In other words, the resulting correlation is comparable to the seis-
74 mogram that would be obtained at the first receiver if there is a source located at
75 the second receiver's location. This approach is referred to as seismic interferom-
76 etry (Wapenaar et al., 2010). Noise cross-correlations are often used to retrieve the
77 surface waves component of the Green's function (Shapiro and Campillo, 2004,
78 and later works). Extracting body waves contributions to the Green's function
79 is more difficult (Poli et al., 2012a). However, it has been shown that ambi-
80 ent noise cross-correlations can be used to image deep targets inside the Earth
81 with body wave reflections (Draganov et al., 2007; Poli et al., 2012b). Inspired
82 by works done in ultrasound imaging (Aubry and Derode, 2009) and optical mi-

83 crosscopy (Badon et al., 2016), a “reflection matrix approach” was introduced to
84 geophysics and used body wave reflection from coda-wave cross-correlations to
85 image the complex medium below Erebus volcano - Antarctica (Blondel et al.,
86 2018). The “reflection matrix approach” allows to image both specular reflectors,
87 corresponding to the boundaries between layers of different propagation veloc-
88 ities, and non-specular reflections generated by a distribution of localized inho-
89 mogeneities. The matrix imaging approach has then been developed to overcome
90 phase distortions for multi-layered media (Lambert et al., 2020a) and strongly
91 heterogeneous media (Badon et al., 2020; Lambert et al., 2021a). Using the same
92 matrix formalism, Touma et al. (2021) analysed ambient noise recorded at a dense
93 array (1108 vertical geophones in 600 m \times 700 m configuration) to image subsur-
94 face properties of the San Jacinto Fault zone (SJFZ) southeast of Anza, California.
95 While Blondel et al. (2018) dealt with imaging problems in the multiple scatter-
96 ing regime in the case of volcanoes, the main challenge in fault zones imaging is
97 the presence of phase distortions, also referred to as aberrations, due to the strong
98 structural heterogeneities within and around the fault zones.

99 The present paper follows the approach of Touma et al. (2021) to derive more
100 detailed 3D images of the SJFZ at depth and to resolve the shallow structure with
101 unprecedented resolution. Touma et al. (2021) computed noise cross-correlations
102 in the (10-20) Hz frequency range. Whereas the cross-correlations provide a re-
103 sponse matrix between sources and receivers located at the surface, the reflec-
104 tion matrix contains the response between sources and receivers that are virtually
105 moved inside the medium by performing focusing operations. This process is gen-
106 erally known as redatuming (Berkhout and Wapenaar, 1993) and it allows local
107 information on the medium’s reflectivity to be retrieved. To project the data in the

108 virtual focused basis, a homogeneous transmission matrix is used with a constant
109 velocity model of 1500 m/s. This velocity was chosen to optimize the focusing
110 as discussed in Touma et al. (2021). The main advantage of this method is that
111 it only requires an approximate estimation of the medium's velocity. Although
112 an incorrect velocity model produces phase distortions (aberrations) in the propa-
113 gated data, the reflection matrix approach allows us to account and correct these
114 aberrations through the distortion matrix concept (Badon et al., 2020; Lambert
115 et al., 2020b, 2021b). From that matrix, the distorted component is extracted and
116 is used to virtually focus back waves inside the medium (see Appendix A). As
117 a result of the correction process, the resolution of the final subsurface images is
118 drastically improved and a three-dimensional image of the subsurface reflectivity
119 is revealed. The derived images represent reflectivity maps of the medium beneath
120 the Clark branch of the SJFZ at the Sage Brush Flat site (Ben-Zion et al., 2015;
121 Roux et al., 2016). The site under study is located in the complex trifurcation area
122 southeast of Anza, California (Fig. 1a). The locations of the surface fault traces
123 are derived from recent detailed studies of the surface geological mapping and
124 shallow geophysical imaging (Wade, 2018; Share et al., 2020). The basic goal of
125 this paper is to interpret the obtained scattering images that exhibit features with
126 higher lateral resolution than conventional seismic investigations. The variability
127 and attenuation of scattered intensity within and around the major fault zone are
128 also discussed.

129 **2. The San Jacinto Fault Zone**

130 The 230 km-long San Jacinto Fault Zone is the most seismically active fault
131 zone in southern California (Hauksson et al., 2012) and is one of several major

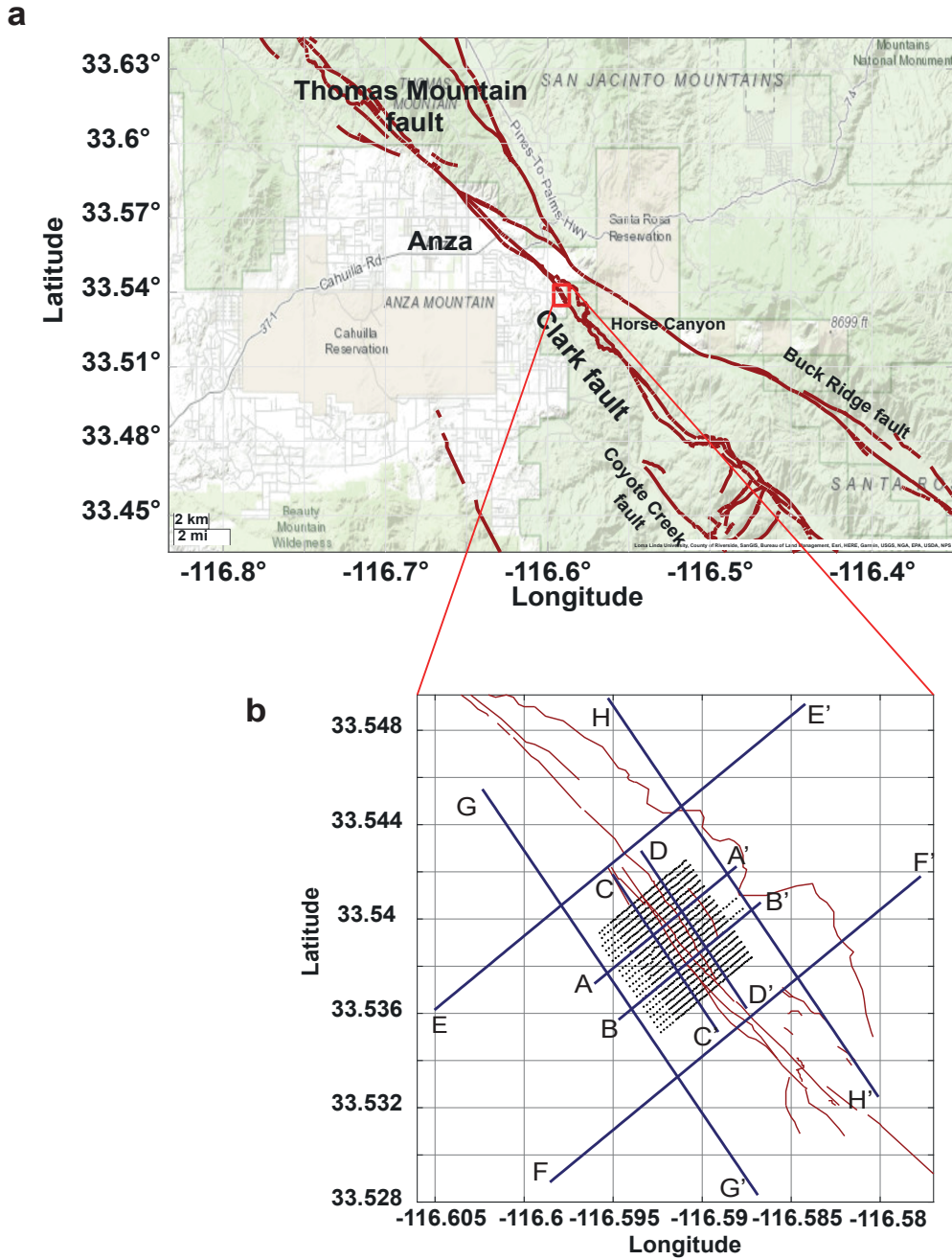


Figure 1: (a) Topographic map of Trifurcation area of San Jacinto fault zone. The red square marks the studied area. (b) Map of the geophones of the dense array at SGB site (black dots). The Clark fault traces are represented by the red lines. The blue lines indicate the locations of the cross-sections represented in Fig. 2 and 3.

132 right-lateral strike-slip fault zones over which the North American-Pacific plate
133 boundary is distributed in southern California. The SJFZ branches from the San
134 Andreas fault at Cajon Pass and was formed 1 – 2 million years ago, presumably
135 in response to the geometrical complexities on the San Andreas Fault in the trans-
136 verse ranges (e.g. Matti and Morton (1993)). The SJFZ represents a less mature
137 evolutionary stage in the life of a large continental strike-slip structure than the
138 San Andreas fault. Approximately 24 km of slip has been accommodated by the
139 SJFZ since the latest Pliocene to early Pleistocene (Dorsey and Roering, 2006),
140 with estimated slip rates that vary along strike between 8 – 20 mm/yr (Rockwell
141 et al., 2003; Fialko, 2006). The SJFZ has varying surface complexity and seismic-
142 ity along its strike. The Anza section to the northwest of the SGB site consists of
143 a single strand, the Clark fault, with relatively regular geometry and low current
144 background microseismicity (Sanders and Kanamori, 1984). The trifurcation area
145 of the SJFZ where the SGB site is located (Fig. 1) is associated with branching
146 of the Clark fault in the Anza section into three major faults: a continuation of
147 the Clark fault and the Buck Ridge and Coyote Creek faults. The Trifurcation
148 area has a broad zone of high seismicity rates that include five earthquakes with
149 magnitudes around 5 since 2001. The geometrical properties of the seismicity in
150 the trifurcation area are very complex and consist of a diffuse pattern in the top 5
151 km that changes to more localized structures dipping to the NE below 6 km, along
152 with zones of seismicity that are orthogonal to the main strike of the SJFZ (Ross
153 et al., 2017).

154 **3. 3D scattering volume**

155 Migration techniques are known to be powerful tools for imaging strong re-
156 flecting boundaries. These boundaries are identified by discontinuities of acoustic
157 impedance in the subsurface and are characterized by specular returns in seis-
158 mic records. Less interest has been accorded to the non-specular component that
159 arises from small-scale geological objects (Khaidukov et al., 2004). The energy
160 generated by such small objects is commonly referred to as diffractions. Non-
161 specular energy holds valuable information on the local heterogeneities in the
162 medium (Schwarz, 2019, and references therein). While many conventional mi-
163 gration techniques, such as Gaussian beam migration and reverse-time migration,
164 honor the diffracted component, such contributions are generally difficult to ana-
165 lyze: they are often suppressed due to the processing done in conventional seismic
166 methods or masked by specular reflections whose amplitudes are much larger than
167 the scattered components (Kozlov et al., 2004). They can also be considered as
168 noise in several migration techniques. Keeping the non-specular component in
169 the analysis allows retrieving signatures of localized scatterers such as cracks or
170 inclusions that lack lateral continuity. Imaging such features whose size is of the
171 order and even smaller than the seismic wavelength contributes significantly to
172 seismic interpretation (Schwarz and Krawczyk, 2020).

173 Fault surfaces and zones with increased fractures density are non-specular ob-
174 jects for surface sensors (Kanasewich and Phadke, 1988). Imaging such features
175 is a challenge in most conventional seismic exploration surveys. Several studies
176 have discussed the necessity of distinguishing between diffractions and reflec-
177 tions, and provided techniques to separate them (Khaidukov et al., 2004; Moser
178 and Howard, 2008; Bakhtiari Rad et al., 2018). Diffraction imaging is performed

179 usually by suppressing the specular reflections so that the migrated image contains
180 the diffracting component that have been isolated. The reflection matrix tech-
181 nique allows us to image, without performing any prior filtering, not only spec-
182 ular reflectors but mainly non-specular backscattered energy that directly gives
183 insight into rock properties at the subsurface. The contribution of specular and
184 non-specular features are distinguishable in the derived images.

185 The constant velocity model of 1500 m/s chosen for the redatuming operation
186 in the initial study of Touma et al. (2021) is highly approximate especially for the
187 deep structure. It was chosen to optimize the focusing at depth with an "apparent"
188 velocity that increases the effective aperture of the geophone array to exploit the
189 actual contribution of multi-scattered paths as discussed in Touma et al. (2021).
190 We recall that a higher velocity will only stretch the detected features vertically.
191 The images are presented as a function of depth for the chosen background veloc-
192 ity and two-way travel time.

193 In the subsequent subsections, we provide a detailed description of cross-
194 sections taken from the 3D scattering volume. Those images are obtained after
195 correcting the aberrations induced by the mismatch between the velocity model
196 used to perform the focusing operation and the data. Although the images shown
197 in Fig. 2 and Fig. 3 will lead to enlightening interpretations, they should be also
198 taken with caution. First, these images have been corrected from transverse aber-
199 rations but axial aberrations can subsist. To cope with this issue, a more accurate
200 2D velocity model can be implemented in the future. Secondly, the aberration
201 correction process applied to these images only identify two isoplanatic patches
202 at each depth. This is probably a perfectible point in such complex heterogeneous
203 media with strong lateral velocity variations. Other less reflective features belong-

204 ing to other isoplanatic patches are thus possibly not revealed by our method in
205 Fig. 2 and 3.

206 A compensation method for attenuation, described in Appendix C, is applied
207 to the reflectivity maps. The results are plotted on a Cartesian grid, with the origin
208 located at the center of the array and the x-axis orthogonal to the fault traces. The
209 colors represent the backscattered intensity plotted in dB. The local distribution of
210 heterogeneities and discontinuities of material boundaries are revealed with max-
211 imal focused intensity. We first present results associated with shallow materials
212 and then discuss deeper structures.

213 We compared our results with previous studies investigating the same region.
214 Most of the studies conducted at the SGB site utilize surface waves to resolve
215 shallow features and the velocity distribution below the dense array (Roux et al.,
216 2016; Hillers et al., 2016; Mordret et al., 2019) or fault zone head waves to image
217 lateral variations of lithology and damage across the fault (Ben-Zion et al., 2015;
218 Qin et al., 2018). To our knowledge, the deep scattering structure has not been
219 examined and analyzed yet.

220 *3.1. Images of the shallow fault zone*

221 The high frequency cross-correlations of noise recorded by the dense array
222 allow resolving features in the top few hundred meters of the crust. Fig. 2 shows
223 vertical slices of the 3D volume with a close-up view of the first 400 m: two slices
224 perpendicular to the fault (AA', BB') and two slices parallel to the fault traces
225 (CC', DD'). For the sake of simplicity, the cross-sections are labeled North, South,
226 West and East, respectively. The slices are plotted in logarithmic dB scale and
227 reveal the backscattered intensity rising from highly reflective features detected
228 through the aberration correction process. The location of the each cross-section

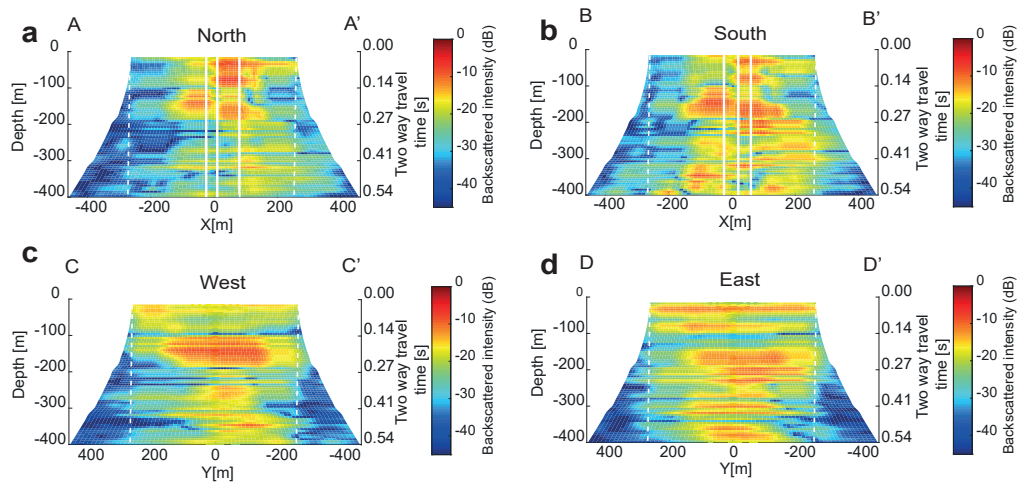


Figure 2: Shallow cross-sections of the 3D scattering volume. Vertical slices oriented perpendicular to the fault traces. North/South denote Northwest and Southeast. The main fault strands are represented by the bold white lines. (a) Profile A-A', (b) Profile B-B'. Vertical slices oriented parallel to the fault traces. West/East denote Southwest and Northeast. (c) Profile C-C', (d) Profile D-D'. The color scale is in dB. The white dashed lines correspond to the spatial extension of the array.

229 is indicated by blue lines in Fig. 1b. In the first two vertical slices, the white lines
230 refer to the location of the three main sub-parallel strands represented in red in
231 Fig. 1b.

232 Several differences between the results in the slices oriented differently stand
233 up. The first thing to notice are the structural variations across the fault zone
234 in Figs. 2a and b. We observe high intensity of scatterers within the core fault
235 damage zone and reduced scatterers intensity outside. A clear offset of reflective
236 structures is observed around a depth of 150 m in the two perpendicular panels.
237 Figs. 2a and b share the same features although the scattering appears stronger
238 and more extended in the southern profile (B-B'). The intensity below 150 m de-
239 creases in the North cross-section while in the South cross-section a high density
240 of scatterers extends to greater depth revealing a localized damage zone around the
241 fault traces (white lines).

242 The offset of the scatterers in Figs. 2a and b is observed mainly below the SW
243 fault trace. Qin et al. (2018) suggested that the SW fault trace is the main seismo-
244 genic fault separating two crustal blocks of different seismic properties. Mordret
245 et al. (2019) also showed the presence of a velocity contrast across the SW fault
246 trace. The observed offset in structural properties can be explained by the fact that
247 the SW trace represents the main seismogenic fault.

248 Figs. 2c and d representing the West and East cross-sections show no clear
249 lateral variations of the subsurface structures. The reflectivity is associated with
250 planar features or layers located on each side of the fault. The high scattering zone
251 to the NE of the surface trace, clearly observed in Fig 2d, is in general agreement
252 with the trapping structure identified by Ben-Zion et al. (2015) and Qin et al.
253 (2018). This zone is characterized by significant low velocities and an intense

254 localized damage producing reflections (Roux et al., 2016; Hillers et al., 2016;
255 Mordret et al., 2019). The reflective layer SW of the fault observed in Fig 2c co-
256 incides with the local sedimentary basin reported by Ben-Zion et al. (2015), Roux
257 et al. (2016) and Hillers et al. (2016).

258 Many studies of the San Jacinto Fault Zone observed an asymmetric rock dam-
259 age across the fault (Lewis et al., 2005; Dor et al., 2006; Qin et al., 2018; Wade,
260 2018). The damage at the SGB site was shown to be greater on the NE side of the
261 fault. The scattering in Fig. 2a is more pronounced in the NE. Between 150 and
262 400 m, the scattering zone dips slightly to the NE and is comparable to the shape
263 of the low velocity trough found by Mordret et al. (2019) beneath the fault trace
264 at the same location as profile AA'.

265 3.2. *Deeper and larger scale structure*

266 We now investigate deeper sections from the 3D volume. Fig. 3 shows four
267 vertical 4 km deep slices; two slices are oriented perpendicular to the fault, one
268 in the Northwest (EE') of the array and the other in the Southeast (FF'), and two
269 additional slices oriented parallel to the fault, one in the Southwest (GG') of the
270 array and the other in the Northeast (HH'). The locations of the cross-sections
271 are marked by blue lines in Fig. 1b. All vertical cross-sections are presented in
272 the form of animated movies in Animation D.1 (slices perpendicular to the fault
273 traces) and Animation .D.2 (slices parallel to the fault traces).

274 In general, reflectors can only be imaged over a transverse field-of-view lim-
275 ited by the size of the geophones' array. Indeed, in the case of planar interfaces,
276 a part of the reflected wave-field is not captured by the geophone array for large
277 angles of incidence (See supplementary Fig. B.1a). Yet, the 3D scattering images
278 shown in Fig. 3 reveal features that extend well beyond the spatial extension of

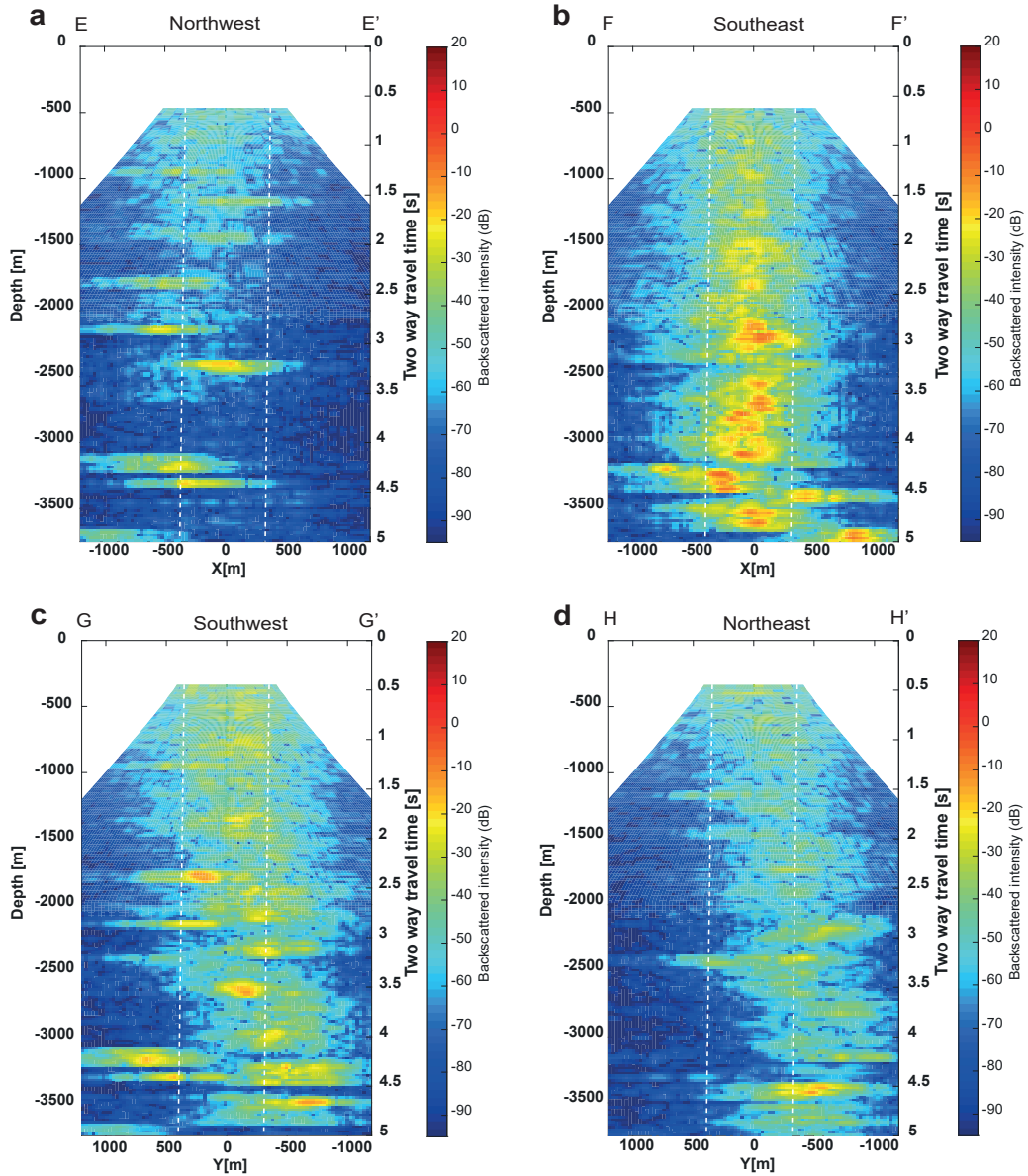


Figure 3: Deep cross-sections of the 3D scattering volume. Vertical slices oriented perpendicular to the fault traces. (a) Profile E-E' Northwest (NW) of the array, (b) Profile F-F' Southeast (SE) of the array. Vertical slices oriented parallel to the fault traces. (c) Profile G-G' Southwest (SW), (d) Profile H-H' Northeast (NE). The color scale is in dB. The white dashed lines correspond to the spatial extension of the array.

279 the array. This observation is made possible due to the intense damage around the
280 fault zone. In such diffusive media, the strong heterogeneities reflect the incident
281 waves in many different directions, and therefore the imaged field-of-view is ex-
282 tended (See supplementary Fig. B.1b). Interfaces between geological layers are
283 also imaged beyond the array extension by means of the waves scattered by the
284 localized heterogeneities that reside at the discontinuity across interfaces.

285 The comparison between the first two panels (Figs. 3a and b) reveals a clear
286 difference in reflectivity between the Northwest (NW) and Southeast (SE) por-
287 tions of the SGB site. Both panels show a broad scattering zone in the shallow
288 crust that has a V shape with about 800 m wide area at $z = 500$ m ($t = 0.7$ s)
289 (Figs. 3a and b). The dense distribution of scatterers in the shallow zone results
290 likely from the heavily damaged rocks around the fault traces. In the NW panel,
291 the diffuse damage is less apparent deeper than $z = 1000$ m ($t = 1.3$ s). However,
292 the observed back-scattered energy in that section is associated with horizontal
293 reflectors emerging on both sides of the fault. Discontinuous blocks on the right
294 and left side of the fault traces highlight the offset of geological features across the
295 fault. In contrast, the high intensity scattering zone extends deeper than $z = 1000$
296 m ($t = 1.3$ s) in the SE slice. Around $z = 1500$ m ($t = 2$ s), the backscattered
297 intensity reveals a zone that is about 450 m wide. Deeper in the crust, scattering
298 seems to persist in combination with specular reflections arising from discontinu-
299 ous deep layers ($z = 3300$ m, $t = 4.4$ s).

300 The different scattering zone extensions in Figs. 3a and b are consistent with a
301 change in the nature and structural complexity of the fault zone in the study area.
302 To the NW of the SGB site, the SJFZ occupies a linear valley, whereas, to the SE,
303 it becomes more localized and is associated with a canyon (Sharp, 1967). Recent

304 geological mapping in the area (Wade 2018) shows multiple fault strands at the
305 SGB site (Fig. 1b). One main fault is mapped at the base of the NW boundary of
306 the SGB basin. To the SE along strike, that fault merges with two other faults and
307 results in a more localized zone that is associated with a higher damage intensity.
308 The reflectivity panels confirm this feature by showing a significant scattering at
309 depth SE of the array related to highly damaged (cracked and crushed) rocks. In
310 the first 2 km ($t = 2.7$ s), the fault appears to be more localized in the SE generat-
311 ing an intense distribution of scatterers. Indeed, the scattered wavefield dominates
312 and the specular component is less apparent in the SE compared with the NW.
313 In the NW, the damage zone is more distributed and less intense. The damage
314 intensity is rapidly decaying with depth, and the spreading of the scattering zone
315 is mainly observed in the first kilometer. At larger depth, specular reflections
316 predominate over the scattered component.

317 The panels oriented parallel to the fault also display a structural difference
318 between the right and left sides of the fault. The scattering appears to be more
319 concentrated in the SW profile (Fig. 3c), whereas the NE profile (Fig. 3d) shows
320 strong continuity of planar boundaries. These observations are also in agreement
321 with (Sharp, 1967, Fig.3) where the SW of the SJFZ at Table Mountain exhibits
322 more complexity than the NE region. The scattering zones in both sections are
323 dipping toward the SE where the fault zone is more localized.

324 In the following, we will show that the reflection matrix contains much more
325 information than the medium's reflectivity. It also provides a direct insight into
326 the variations of the scattering properties and the attenuation of scattered waves in
327 the fault region.

328 **4. Lateral variations of intensity**

329 Seismic waves propagating inside the Earth give direct insight on the nature
330 and properties of rocks. While travelling through complex heterogeneous media,
331 waves suffer from seismic attenuation. In this section we briefly discuss seismic
332 wave attenuation principles and how attenuation is accounted for in our matrix
333 formalism, and therefore in the images obtained.

334 Seismic attenuation describes the decay of energy experienced by seismic
335 waves while they propagate. Amplitudes are easily altered by several factors such
336 as geometrical spreading, scattering and absorption (intrinsic or anelastic attenua-
337 tion) (Shapiro and Kneib, 1993; Knipe et al., 1998). Evaluation of the attenuation
338 due to scattering and intrinsic absorption has been the subject of considerable stud-
339 ies in seismology (Aki, 1969; Sato et al., 2012). Estimating attenuation properties
340 provides complementary information to seismic velocity distribution, and can be
341 particularly useful in fault zone studies to obtain a better understanding of rock
342 properties and subsurface structures. Within the framework of the present paper,
343 seismic attenuation is being examined to: (i) compensate the intensity decay in the
344 3D volume (see Appendix C) and (ii) reveal lateral variability of backscattered
345 intensity in the fault zone.

346 The intensity represented in the pixels gives a direct estimate of the scattering
347 properties in the region. To detect possible lateral variability of the energy distri-
348 bution below the dense array, we divide the area into sub-regions and examine the
349 intensity of temporal decay for shallow and deep parts. In Fig. 4a, the study area is
350 divided into three zones displayed in Fig. 4a1: a zone representing the main fault
351 zone (red shaded area), a region to the SW of the fault zone (blue shaded area)
352 and a region to the NE of the fault zone (green shaded area). For each region, we

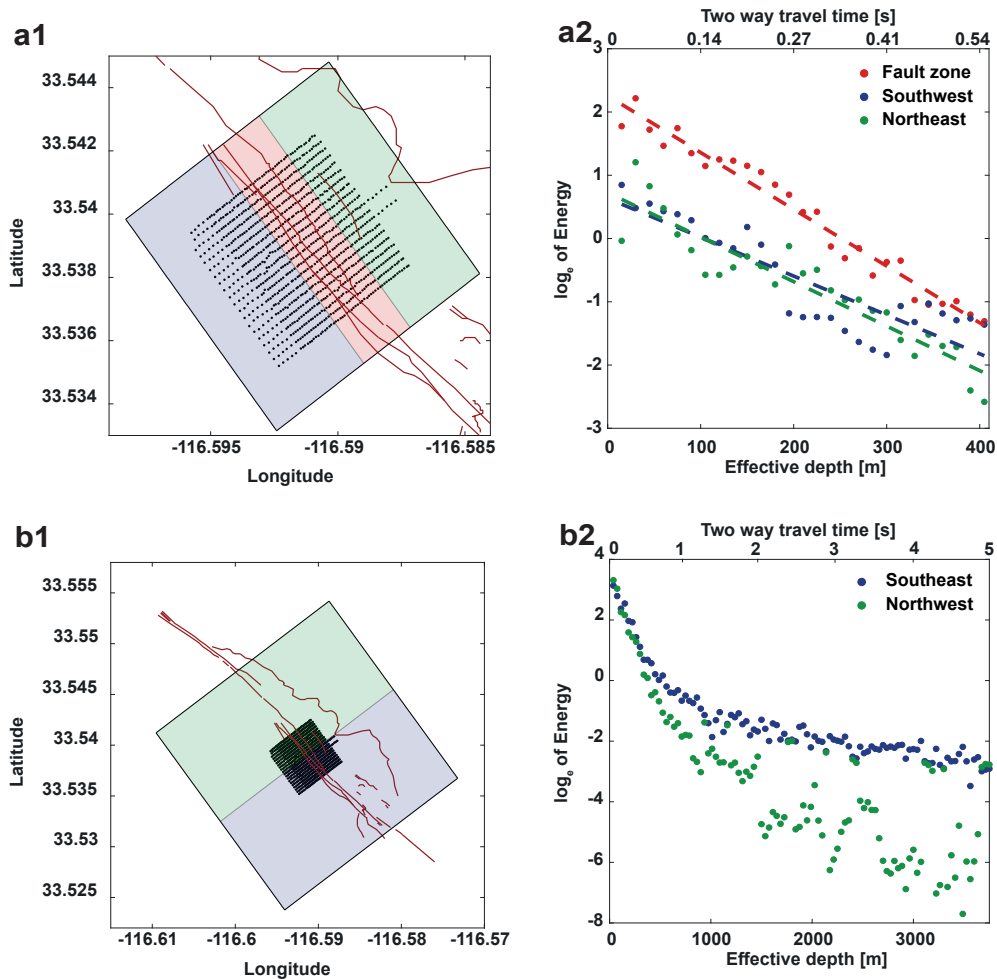


Figure 4: Time decay of the backscattered intensity. (a) Lateral variation of the time decay in the shallow crust for the first 400 m. The area is discretized into three zones: red color refer to the fault zone, blue color to the SW and green color to the NE. (b) NW - SE variation of the backscattered intensity time decay in the deep crust up to 4000 m. The area is discretized in two zones: blue color refers to the SE and green color to the NW. (1) Map of the geophones of the dense array at SGB site (black dots). The Clark fault traces are represented by the red lines. The black rectangle corresponds to the area covered by the images. (2) Intensity decay as a function of apparent depth and, equivalently, of two way travel time of the scattering volume.

353 compute the mean intensity of the pixels located beneath that region. The energy
354 distribution for the first 400 m is presented in Fig. 4a2. The linear regression is
355 also plotted (dashed lines) to visualize the slope of the energy decay. We only
356 show the energy decay corresponding to the images after the correction process.
357 The first noticeable feature is that the fault zone is associated with higher intensity
358 values resulting from non-specular energy transmitted from the localized damage.
359 This is consistent with the overall amplification of seismic waves in low velocity
360 fault zone layers (e.g. Kurzon et al. (2014)). The energy in the fault zone with a
361 steep slope distinguishes itself from the surrounding western and eastern regions
362 where the decay slopes are more gradual. The fault zone is defined by major
363 fracturing and crushed rocks, and consequently it is characterized by a rapid en-
364 ergy decay. In the neighboring regions where the damage is more distributed, less
365 attenuation is observed in comparison with the fault zone. These results are con-
366 sistent with significantly lower values of attenuation coefficients generally found
367 within fault zones by waveform fitting of trapped waves (e.g. Lewis et al. (2005);
368 Qin et al. (2018)).

369 We also compare the intensity decay between the SE and NW sections 4 km
370 below the array. Fig. 4b2 shows plots of the backscattered intensity averaged
371 across the two regions delineated in Fig. 4b1. We choose to plot the measured
372 intensity values without the linear regression. The discrepancy observed in the
373 backscattered intensity distribution primarily reflects the difference in subsurface
374 structure between the two regions that was highlighted in section 3.2. The fluc-
375 tuation of intensity in the NW plot (green dots) is associated with the specular
376 returns at several depths. In other words, high values correspond to the reflective
377 boundaries observed in Fig. 3a, while the blue scatter plot representing the SE of

378 the array decreases smoothly. This is explained by the consistent density of scat-
379 terers around the core of the fault zone damage area previously highlighted by the
380 cross section in Fig. 3b.

381 **5. Discussion and conclusions**

382 The presented results provide detailed images of seismic properties in the 3D
383 volume around the San Jacinto fault at the SGB site. We used one month of
384 ambient seismic noise recorded by a dense array deployed at SGB site around the
385 Clark branch of SJFZ. The high frequency seismic data provided by the spatially
386 dense array allows us to resolve features near the surface with high resolution.
387 The reflectivity maps representing slices of the 3D scattering volume are obtained
388 through the reflection matrix procedure developed in Touma et al. (2021). Body
389 wave reflections from ambient noise correlations are used to image the fault zone
390 structure up to 4 km below the surface. These images reveal the backscattered
391 intensity generated by the distribution of heterogeneities in the medium.

392 Fault zones are very complex regions with extensive fracturing and damage
393 that can reach the bottom of the seismogenic zone in some places as seen in to-
394 mographic studies around large faults (e.g. Allam et al. (2014)). Tomographic and
395 other imaging studies provide average properties of rock volumes, but do not re-
396 solve the presence, location and intensity of scatterers that are imaged with the re-
397 flection matrix method. The strong variations of velocities and significant attenua-
398 tion in fault zone regions present challenges for conventional imaging techniques.
399 However, our reflection matrix approach allows us to derive the distribution of
400 scatterers inside the medium with an approximate velocity model of the medium.
401 To that aim, a powerful aberration correction process is performed and provides

402 high resolution images of the subsurface. However, associating a reflector with
403 a specific depth remains dependent on the reference velocity model, so the re-
404 flectivity maps are displayed as a function of an effective depth and the observed
405 two-way travel time.

406 A significant advantage of the matrix approach is that focusing inside the
407 medium enables the imaging of not only specular reflectors but also of scattering
408 objects such as cracks and fractures. While many methods consider the diffracting
409 and scattering components as noise in the seismic data, and tend to remove these
410 components to image discontinuous layers, the current approach takes advantage
411 of the scattering in the complex fault zone to resolve features of the order of the
412 wavelength. This constitutes one of the main strength of the method. The images
413 in Figs. 2 and 3 show both discontinuities of some layers that are signature of a
414 large fault, along with lateral and axial variations in the backscattered intensity
415 induced by cracks and other small-scale heterogeneities. The axial variations of
416 the backscattered intensity in Fig. 4 also reveal systematic differences in scatter-
417 ing properties in the region within and around the surface fault traces relative to
418 the outside volume, as well as differences between the NW and SE portions of the
419 study area. The results are consistent with more localized intense damage zone at
420 depth in the SE section where the SJFZ enters the Horse canyon, and more diffuse
421 rock damage to the NW where the SJFZ is in a linear valley. The higher damage
422 at depth in the SE section also suggests a geometrical complexity at depth lead-
423 ing to an ongoing generation of rock damage that is overprinted on older healed
424 damage (Sharp, 1967).

425 Fig. 5 summarized schematically the obtained imaging results for both the
426 inner and outer damage zones in the area. The fault traces in Fig. 1a suggest a

427 broader and less intense fault zone in the NW than in the SE. Surface observations
428 are consistent with the fact that the main fault and the surrounding core damage
429 are more localized in the SE where the principle slip zone is delineated by in-
430 tense damage and fracturing extending down to 3 to 4 kilometers. In the NW, the
431 scattering in the FZ is only observed in the first kilometer indicating a shallow
432 less intense and diffuse damage. The results in Figs. 3c and d show that the dam-
433 age distribution is more complex to the SW side of the fault exhibiting a more
434 pronounced outer damage in the SW than in the NE side of the fault.

435 The lateral variations of the fault structure between the NW and SE are consis-
436 tent with the transition from the Anza section of the SJFZ associated with a single
437 major fault trace, to a complex fault zone in the trifucation area with several traces
438 at the surface. The high scattering zone that extended to depth in the SE part of
439 the SGB site is likely associated with highly damaged fault zone rocks between
440 the sub-parallel strands in the SE.

441 **Acknowledgments**

442 We acknowledge support from the European Research Council (ERC) un-
443 der the European Union Horizon 2020 research and innovation program (grant
444 agreement No 742335, F-IMAGE and grant agreement No. 819261, REMINIS-
445 CENCE). YBZ acknowledges support from the Department of Energy (Award
446 DE-SC0016520). The study was funded primarily by LABEX WIFI (Laboratory
447 of Excellence within the French Program Investments for the Future, ANR-10-
448 LABX-24 and ANR-10-IDEX-0001-02 and by TOTAL R&D. The paper bene-
449 fitted from constructive comments by two anonymous referees and Editor Rebecca
450 Bendick

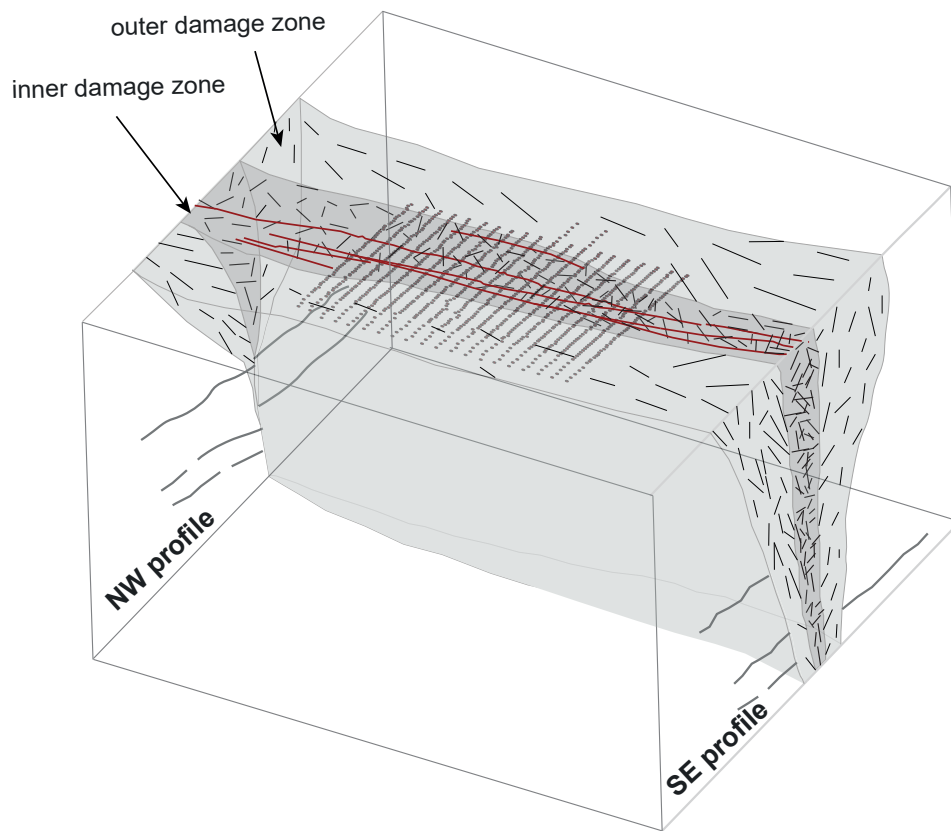


Figure 5: Schematic illustration of the fault zone at SGB site. Black dots refer to the geophones and red lines represent the Clark fault traces.

451 **DATA AVAILABILITY**

452 The seismic data used in this study can be obtained from the Data Manage-
453 ment Center of the Incorporated Research Institutions for Seismology (IRIS). The
454 facilities of IRISData Services, and specifically the IRIS Data Management Cen-
455 ter, were used for access to waveforms, related metadata, and/or derived products
456 used in this study. IRIS Data Services are funded through the Seismological Facil-
457 ities for the Advancement of Geoscience (SAGE) Award of the National Science
458 Foundation under Cooperative Support Agreement EAR-1851048.

459 **Appendix A. Imaging and aberration correction**

460 In this section, we review the reflection matrix technique (Touma et al., 2021)
461 applied to obtain the 3D scattering images of the accompanying paper. First we
462 describe the virtual focusing method inside the medium and then we recall the
463 aberration correction process.

464 Ambient noise cross-correlations between the stations are computed in the
465 10-20 Hz range. These correlations provide the impulse response between vir-
466 tual sources (emission) and receivers (reception) at the surface. In other words,
467 the cross-correlations form a response matrix $\mathbf{K}(t)$ of the underground associated
468 with the geophones' array. This matrix contains considerable of information about
469 the medium, especially the distribution of its local reflectivity. This information
470 is retrieved from the response matrix by performing focusing operations, both in
471 emission and reception. Focusing consists in applying appropriate time delays, at
472 emission and reception, so that the seismic waves resulting from a scattering event
473 at the focal point interfere constructively. The goal of this operation is to virtu-
474 ally move the sources and receivers inside the medium onto a virtual plane. It is

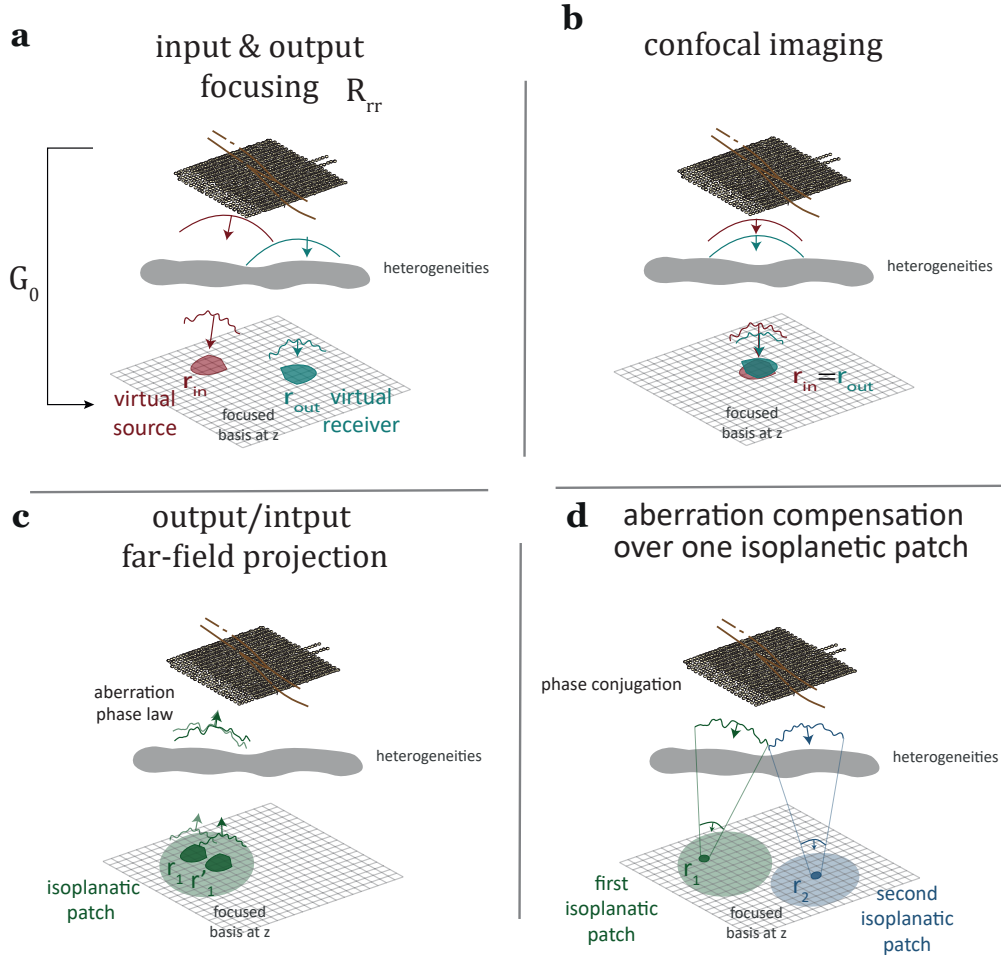


Figure A.1: Focused reflection matrix and aberration correction. (a) The response matrix is projected onto a focused basis at depth z both at emission (in) and reception (out). The focusing points synthesise virtual sources and receivers scanning every point in the virtual plane. In the presence of heterogeneities, the waves are distorted and the focusing is not optimal. (b) Confocal imaging principle: The image of the medium is obtained when input and output focusing are performed at the same location in the focused basis. (c) Far-field projection of the focused reflection matrix: For each virtual source, the reflected wave-front is investigated in the far-field. The phase distortions are identical for nearby virtual sources belonging to the same isoplanatic patch. (d) The phase conjugate of the aberration phase law enables a fine compensation of aberrations over the corresponding isoplanatic patch.

475 commonly referred to as redatuming (Berkhout and Wapenaar, 1993) and can be
476 easily implemented in the frequency domain via simple matrix products. The first
477 step is to apply a temporal Fourier transform to the correlation matrix to obtain
478 $\mathbf{K}(f)$.

479 To perform focusing, we define at each depth a basis of focal points \mathbf{r} , which
480 corresponds to the location of virtual geophones inside the medium. A constant
481 velocity model of 1500 m/s is chosen for the transmission matrix $\mathbf{G}_0(f)$ that
482 describes the propagation of waves between the surface and the focused basis.
483 At each frequency, the response matrix is projected into the focused basis both
484 in emission and reception (Fig. A.1a). The broadband focused reflection matrix
485 $\mathbf{R}_{\mathbf{r}\mathbf{r}}(z)$ is then computed by calculating the coherent sum of the focused reflection
486 matrices over the considered frequency range. This last operation amounts to a
487 ballistic time gating of singly-scattered waves at time $t \sim 2z/c_0$. The coefficients
488 $\mathbf{R}(\mathbf{r}_{\text{out}}, \mathbf{r}_{\text{in}})$ of this matrix correspond to the responses between a set of virtual
489 sources $\mathbf{r}_{\text{in}} = (x_{\text{in}}, y_{\text{in}}, z)$ and receivers $\mathbf{r}_{\text{out}} = (x_{\text{out}}, y_{\text{out}}, z)$ at each depth z .
490 Among all these coefficients, the diagonal elements ($\mathbf{r}_{\text{in}} = \mathbf{r}_{\text{out}}$), are of particular
491 interest since they provide a confocal image of the underground (Fig. A.1b). The
492 other coefficients of $\mathbf{R}_{\mathbf{r}\mathbf{r}}$ are also useful since the focusing quality can be directly
493 quantified by the spreading of the backscattered energy over its off-diagonal ele-
494 ments. In the presence of strong phase distortions (aberrations), resulting from a
495 very complex seismic velocity distribution, each input and output focal spot can
496 actually spread well beyond the diffraction limit, giving rise to a loss of resolution
497 and contrast of the confocal image. Interestingly, the reflection matrix can also
498 be used to retrieve in post-processing the shape of wave-fronts that would allow
499 a perfect compensation for these phase distortions. To do so, one can exploit the

500 spatial correlations that exist between the phase distortions undergone by the re-
501 flected wave-fronts induced by nearby virtual geophones. This coherence area is
502 referred to the isoplanatic patch (Fig. A.1c). The idea is to project the focused
503 reflection matrix at input or output in a basis that maximizes the size of such iso-
504 planatic patches in the focal plane. For a multi-layered basis, the most adequate
505 basis is the Fourier basis (k) that amounts to projecting the reflected wave-field
506 in the far-field. The aforementioned spatial correlations are then leveraged by
507 extracting the distorted component of each reflected wave-field. It results in a dis-
508 tortion matrix whose singular value decomposition provides a decomposition of
509 the field-of-view into a set of isoplanatic patches with the associated aberration
510 phase transmittances. The phase conjugate of each aberration phase law provides
511 the focusing law that should be used to compensate for aberrations on each iso-
512 planatic patch (Fig. A.1d). Such a focusing law is applied here to the reflection
513 matrix from the dual basis to obtain an updated focused reflection matrix. A cor-
514 rected confocal image is obtained by considering the diagonal coefficients of this
515 new focused reflection matrix.

516 The whole process can be iterated at input and output in order to refine our
517 estimation of the focusing law over each isoplanatic patch. To that aim, the fo-
518 cused reflection matrix should be projected in the far-field (Fourier basis k) by
519 switching, at each iteration, between input or output.

520 **Appendix B. Specular vs. diffuse reflection**

521 The finite size of the geophone array has an impact on the field-of-view that
522 can be imaged by the reflection matrix approach. To quantify this effect, two
523 synthetic tests have been performed: (i) considering planar reflectors at a given

524 depth $z = 3600m$ (specular scattering, see Fig. B.1a1); (ii) considering randomly
525 distributed scatterers at the same depth (diffuse scattering, see Fig. B.1b1). In
526 each case, an homogeneous effective wave velocity $c_0 = 1500m/s$ is considered.
527 Fig. B.1a2 and B.1b2 show the results of the numerical simulations.

528 Fig. B.1a2 shows a synthetic confocal image obtained for the specular reflec-
529 tor. The field-of-view is limited by the size of the array. The fraction of the inci-
530 dent wave-front that spreads beyond the transverse size of the array gives rise to
531 reflected waves that cannot be recorded by the array of geophones (red arrows in
532 Fig. B.1a1). Fig. B.1b2 displays the field-of-view of our matrix imaging method
533 in the diffuse scattering regime. This intensity distribution is obtained by averag-
534 ing the synthetic confocal image over a number $N = 50$ realizations of disorder.
535 Unlike for specular reflectors, incident wave-fronts are reflected in different direc-
536 tions (arrows in Fig. B.1b1). Consequently, the field-of-view spreads well beyond
537 the transverse size of the geophone's array. The latter observation explains the
538 wide field-of-view obtained in the 3D-scattering images of the accompanying pa-
539 per (Fig. 3). The reflection matrix method mainly images a distribution of small
540 heterogeneities that are located in the damage area at shallow depths ($z < 1500m$)
541 and that reside between each geological layer at larger depths.

542 **Appendix C. Time-gain compensation**

543 The energy losses increase with the heterogeneity of the medium. The prop-
544 agation matrix used to project the raw data to the focused basis accounts for ge-
545 ometrical spreading whereas the effect of absorption and scattering are ignored.
546 In particular, in strong scattering regime, these losses can strongly degrade the
547 contrast of the images at larger depth. To overcome these problems in the imag-

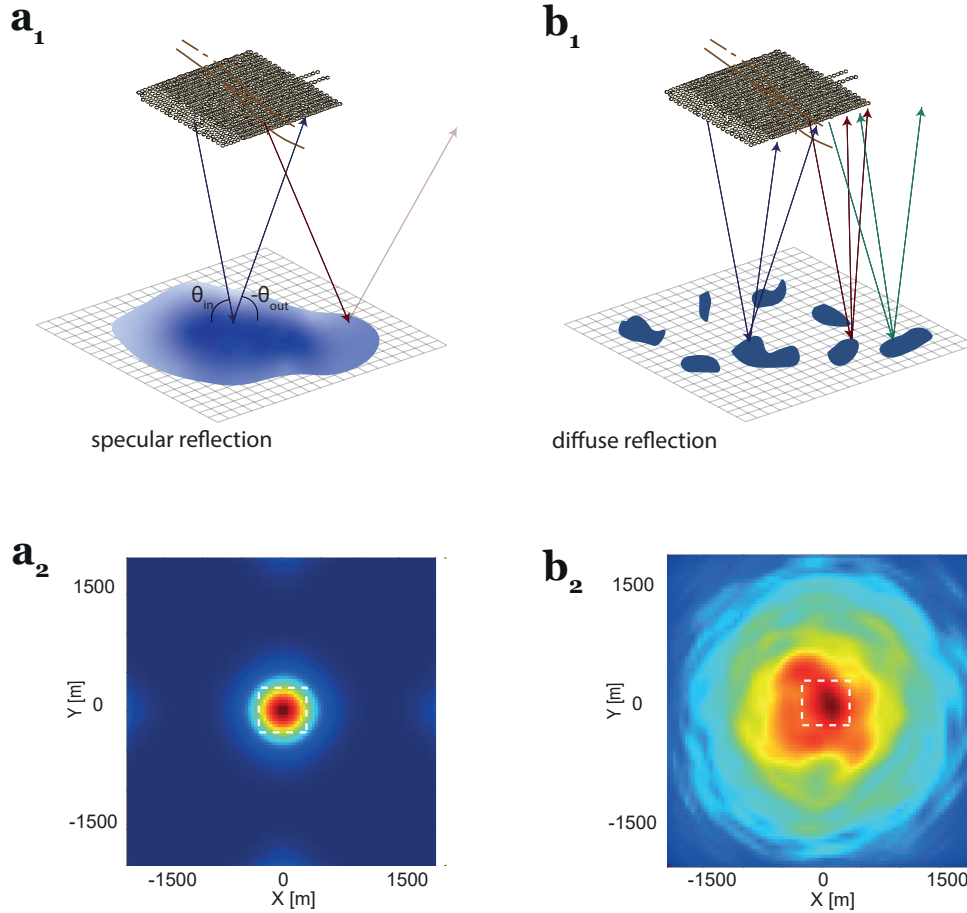


Figure B.1: Impact of specular and diffuse reflection on the field-of-view of the confocal image. (a) Smooth mirror-like surface. (a.1) Sketch showing the reflected waves traveling with the same angle as the incident waves. Some of the reflected rays are not captured by the array. (a.2) Synthetic confocal image of a specular reflector at $z = 3600$ m. The white dashed square corresponds to the spatial extension of the array. (b) Random scattering medium. (b.1) Sketch displaying distributed heterogeneities at depth. An incident ray is scattered in all directions enabling a confocal image that extends well beyond the lateral dimensions of the geophone array. (b.2) Mean synthetic confocal image at $z = 3600$ m estimated from several iterations obtained in the case of a random medium. The white dashed square corresponds to the spatial extension of the array. The imaged field-of view extends well beyond the transverse size of the array.

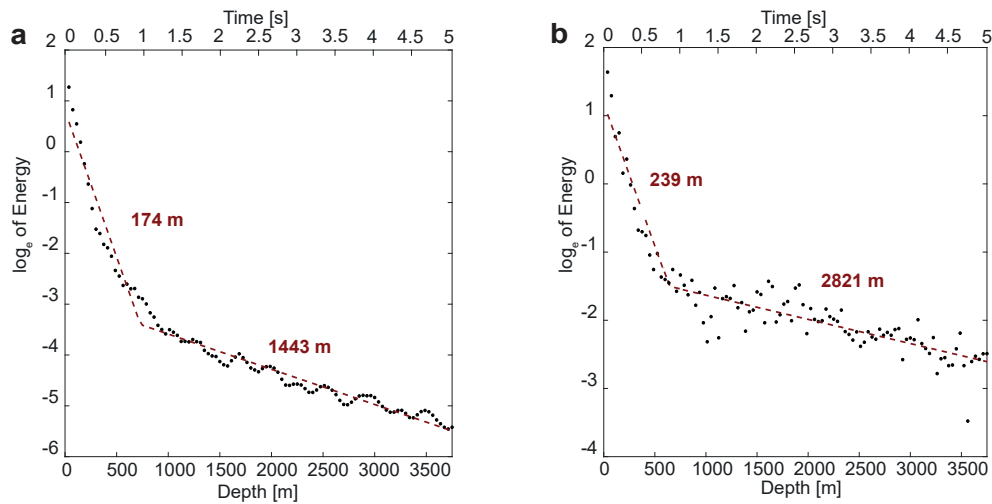


Figure C.1: Mean intensity decay as a function of depth with the corresponding linear regression in logarithmic scale and the characteristic length of decay values. (a) Intensity decay of raw images. (b) Intensity decay of images corrected from the aberrating component.

548 ing process and in order to visualize the entire field-of-view, it is mandatory to
 549 compensate for the amplitude drop in the 3D-images (Fig. 2 and 3), especially in
 550 the shallow crust. This time gain compensation is done manually by multiplying
 551 the intensity profiles by an increasing function with depth, that is in this case the
 552 reciprocal of the mean intensity calculated at each depth.

553 An estimation of the seismic wave attenuation at the SGB site can be directly
 554 measured through the backscattered intensity at each depth. The energy is ob-
 555 tained by calculating the mean square of the intensity of the image pixels, i.e.
 556 the intensity of the diagonal of the reflection matrix. The amplitude decay of
 557 the energy is expected to follow an exponential decaying as a function of depth
 558 (Fig. C.1).

559 Figs. C.1a and b displays the natural logarithm applied to the mean intensity

560 as a function of depth calculated from the raw reflection matrix and the corrected
561 reflection matrix respectively (aberration correction process disclosed in Touma
562 et al. (2021)). In the logarithmic scale, the mean confocal energy is expressed as
563 a decreasing linear line. The characteristic length of attenuation, that corresponds
564 to the inverse of the slope of the log-energy decay, is also shown.

565 A change of slope is observed in both plots corresponding to depth of 750 m
566 ($t = 1$ s). While a pronounced decrease in intensity occurs until 750 m, a more
567 gentle slope is noticed below 750 m. The presence of stratigraphic boundaries, ab-
568 sorbing sediments and intense fracturing is a possible cause of the high attenuation
569 observed at shallow layers. Another thing to notice is the increase by around twice
570 the characteristic length values after correction. We recall that the energy decay
571 describes the losses that the seismic waves undergo while propagating inside the
572 medium. In case of strong inhomogeneities and velocity variation, the wavefield
573 is heavily distorted and the focusing inside the medium fails. The increase in the
574 slope provided by the aberration correction process indicates an improvement in
575 the focusing operation and consequently an enhancement of the detection.

576 **Appendix D. Supplementary Data**

577 Supplementary data associated with this article can be found in the online
578 version.

579 Animation D1: Animated vertical slices oriented perpendicular to the fault
580 traces.

581 Animation D2: Animated vertical slices oriented parallel to the fault traces.

582 **References**

- 583 Aki, K., 1969. Analysis of the seismic coda of local earthquakes as scattered
584 waves. *J. Geophys. Res.* 74, 615–631.
- 585 Allam, A., Ben-Zion, Y., Kurzon, I., Vernon, F., 2014. Seismic velocity structure
586 in the hot springs and trifurcation areas of the san jacinto fault zone, california,
587 from double-difference tomography. *Geophys. J. Int* 198, 978–999.
- 588 Aubry, A., Derode, A., 2009. Detection and imaging in a random medium: A ma-
589 trix method to overcome multiple scattering and aberration. *Journal of Applied*
590 *Physics* 106, 044903.
- 591 Badon, A., Barolle, V., Irsch, K., Boccara, A.C., Fink, M., Aubry, A., 2020. Dis-
592 tortion matrix concept for deep imaging in optical coherence microscopy. *Sci.*
593 *Adv.* 6, eaay7170.
- 594 Badon, A., Li, D., Lerosey, G., Boccara, A.C., Fink, M., Aubry, A., 2016. Smart
595 optical coherence tomography for ultra-deep imaging through highly scattering
596 media. *Sci. Adv.* 2, e1600370.
- 597 Bakhtiari Rad, P., Schwarz, B., Gajewski, D., Vanelle, C., 2018. Common-
598 reflection-surface-based prestack diffraction separation and imaging. *Geo-*
599 *physics* 83, S47–S55.
- 600 Ben-Zion, Y., 2008. Collective behavior of earthquakes and faults: Continuum-
601 discrete transitions, progressive evolutionary changes, and different dynamic
602 regimes. *Rev. of Geophys.* 46.

- 603 Ben-Zion, Y., Sammis, C.G., 2003. Characterization of fault zones. *Pure and*
604 *applied geophysics* 160, 677–715.
- 605 Ben-Zion, Y., Vernon, F.L., Ozakin, Y., Zigone, D., Ross, Z.E., Meng, H., White,
606 M., Reyes, J., Hollis, D., Barklage, M., 2015. Basic data features and results
607 from a spatially dense seismic array on the San Jacinto fault zone. *Geophys. J.*
608 *Int.* 202, 370–380. doi:10.1093/gji/ggv142.
- 609 Berkhout, A.J., Wapenaar, C.P.A., 1993. A unified approach to acoustical reflec-
610 tion imaging. II: The inverse problem. *J Acoust. Soc. Am.* 93, 2017–2023.
- 611 Binet, R., Bollinger, L., 2005. Horizontal coseismic deformation of the 2003 bam
612 (iran) earthquake measured from spot-5 thr satellite imagery. *Geophys. Res.*
613 *Let.* 32.
- 614 Blondel, T., Chaput, J., Derode, A., Campillo, M., Aubry, A., 2018. Matrix ap-
615 proach of seismic imaging: application to the Erebus volcano, Antarctica. *J.*
616 *Geophys. Res.: Solid Earth* 123, 10,936–10,950.
- 617 Campillo, M., Roux, P., 2014. Seismic imaging and monitoring with ambient
618 noise correlations. *Treatise on Geophysics* 1, 256–271.
- 619 Chester, F.M., Evans, J.P., Biegel, R.L., 1993. Internal structure and weakening
620 mechanisms of the san andreas fault. *J. Geophys. Res.: Solid Earth* 98, 771–
621 786.
- 622 Dor, O., Rockwell, T.K., Ben-Zion, Y., 2006. Geological observations of damage
623 asymmetry in the structure of the san jacinto, san andreas and punchbowl faults
624 in southern california: A possible indicator for preferred rupture propagation
625 direction. *Pure and App. Geophy.* 163, 301–349.

- 626 Dorsey, R.J., Roering, J.J., 2006. Quaternary landscape evolution in the san jac-
627 into fault zone, peninsular ranges of southern california: Transient response to
628 strike-slip fault initiation. *Geomorphology* 73, 16–32.
- 629 Draganov, D., Wapenaar, K., Mulder, W., Singer, J., Verdel, A., 2007. Retrieval of
630 reflections from seismic background-noise measurements. *Geophys. Res. Lett.*
631 34.
- 632 Etgen, J., Gray, S.H., Zhang, Y., 2009. An overview of depth imaging in explo-
633 ration geophysics. *Geophysics* 74, WCA5–WCA17.
- 634 Fialko, Y., 2006. Interseismic strain accumulation and the earthquake potential on
635 the southern san andreas fault system. *Nature* 441, 968–971.
- 636 Hauksson, E., Yang, W., Shearer, P.M., 2012. Waveform relocated earthquake
637 catalog for southern california (1981 to june 2011). *Bulletin of the Seis. Soc.*
638 of Amer. 102, 2239–2244.
- 639 Hillers, G., Roux, P., Campillo, M., Ben-Zion, Y., 2016. Focal spot imaging based
640 on zero lag cross-correlation amplitude fields: Application to dense array data
641 at the San Jacinto fault zone. *J. Geophys. Res.: Solid Earth* 121, 8048–8067.
- 642 Kanasewich, E.R., Phadke, S.M., 1988. Imaging discontinuities on seismic sec-
643 tions. *Geophysics* 53, 334–345.
- 644 Khaidukov, V., Landa, E., Moser, T.J., 2004. Diffraction imaging by focusing-
645 defocusing: An outlook on seismic superresolution. *Geophysics* 69, 1478–
646 1490.

- 647 Knipe, R.J., Jones, G., Fisher, Q., 1998. Faulting, fault sealing and fluid flow in
648 hydrocarbon reservoirs: an introduction. Geological Society, London, Special
649 Publications 147, vii–xxi.
- 650 Kozlov, E., Barasky, N., Korolev, E., Antonenko, A., Koshchuk, E., 2004. Imaging
651 scattering objects masked by specular reflections, in: SEG Technical Program
652 Expanded Abstracts 2004. Society of Exploration Geophysicists, pp. 1131–
653 1134.
- 654 Kurzon, I., Vernon, F.L., Ben-Zion, Y., Atkinson, G., 2014. Ground motion pre-
655 diction equations in the san jacinto fault zone: Significant effects of rupture
656 directivity and fault zone amplification. *Pure and App. Geophys.* 171, 3045–
657 3081.
- 658 Lambert, W., Cobus, L.A., Couade, M., Fink, M., Aubry, A., 2020a. Reflection
659 matrix approach for quantitative imaging of scattering media. *Phys. Rev. X* 10,
660 021048. `arXiv:eprint number here`.
- 661 Lambert, W., Cobus, L.A., Frappart, T., Fink, M., Aubry, A., 2020b. Distortion
662 matrix approach for ultrasound imaging of random scattering media. *Proc. Nat.*
663 *Sci. Acad.* 117, 14645–14656.
- 664 Lambert, W., Cobus, L.C., Fink, M., Aubry, A., 2021a. Ultrasound matrix imag-
665 ing. I. The focused reflection matrix and the F-factor for a local quantification
666 of aberrations. `arxiv: 2103.02029` .
- 667 Lambert, W., Cobus, L.C., Frappart, T., Fink, M., Aubry, A., 2021b. Ultrasound
668 matrix imaging. ii. the distortion matrix for a local correction of aberrations.
669 `arXiv: 2103.02036` .

- 670 Lewis, M., Peng, Z., Ben-Zion, Y., Vernon, F., 2005. Shallow seismic trapping
671 structure in the san jacinto fault zone near anza, california. *Geophys. J. Int* 162,
672 867–881.
- 673 Manighetti, I., Campillo, M., Sammis, C., Mai, P., King, G., 2005. Evidence
674 for self-similar, triangular slip distributions on earthquakes: Implications for
675 earthquake and fault mechanics. *J. Geophys. Res.: Solid Earth* 110.
- 676 Massonnet, D., Rossi, M., Carmona, C., Adragna, F., Peltzer, G., Feigl, K.,
677 Rabaute, T., 1993. The displacement field of the landers earthquake mapped
678 by radar interferometry. *Nature* 364, 138–142.
- 679 Matti, J.C., Morton, D., 1993. Extension and contraction within an evolving di-
680 vergent strike-slip fault complex: The san andreas and san jacinto fault zones
681 at their convergence in southern california. *The San Andreas fault system: Dis-*
682 *placement, palinspastic reconstruction, and geologic evolution* 178, 217.
- 683 Mitchell, T., Faulkner, D., 2009. The nature and origin of off-fault damage sur-
684 rounding strike-slip fault zones with a wide range of displacements: A field
685 study from the atacama fault system, northern chile. *Jour. of Struct. Geo.* 31,
686 802–816.
- 687 Mordret, A., Roux, P., Boué, P., Ben-Zion, Y., 2019. Shallow three-dimensional
688 structure of the San Jacinto fault zone revealed from ambient noise imaging
689 with a dense seismic array. *Geophys. J. Int.* 216, 896–905.
- 690 Moser, T., Howard, C., 2008. Diffraction imaging in depth. *Geophysical Prospect-*
691 *ing* 56, 627–641.

- 692 Poli, P., Campillo, M., Pedersen, H., Group, L.W., et al., 2012b. Body-wave
693 imaging of earth's mantle discontinuities from ambient seismic noise. *Science*
694 338, 1063–1065.
- 695 Poli, P., Pedersen, H., Campillo, M., 2012a. Emergence of body waves from
696 cross-correlation of short period seismic noise. *Geophys. J. Int.* 188, 549–558.
- 697 Qin, L., Ben-Zion, Y., Qiu, H., Share, P., Ross, Z., Vernon, F., 2018. Internal
698 structure of the san jacinto fault zone in the trifurcation area southeast of anza,
699 california, from data of dense seismic arrays. *Geophys. J. Int.* 213, 98–114.
- 700 Rockwell, T.K., Ben-Zion, Y., 2007. High localization of primary slip zones in
701 large earthquakes from paleoseismic trenches: Observations and implications
702 for earthquake physics. *J. Geophys. Res.: Solid Earth* 112.
- 703 Rockwell, T.K., Young, J., Seitz, G., Meltzner, A., Verdugo, D., Khatib, F., Rag-
704 ona, D., Altangerel, O., West, J., 2003. 3,000 years of groundrupturing earth-
705 quakes in the anza seismic gap, san jacinto fault, southern california: Time to
706 shake it up. *Seismol. Res. Lett.* 74, 236–237.
- 707 Ross, Z.E., Hauksson, E., Ben-Zion, Y., 2017. Abundant off-fault seismicity and
708 orthogonal structures in the san jacinto fault zone. *Sci. Adv.* 3, e1601946.
- 709 Roux, P., Moreau, L., Lecointre, A., Hillers, G., Campillo, M., Ben-Zion, Y.,
710 Zigone, D., Vernon, F., 2016. A methodological approach towards high-
711 resolution surface wave imaging of the San Jacinto Fault Zone using ambient-
712 noise recordings at a spatially dense array. *Geophys. J. Int.* 206, 980–992.
713 doi:10.1093/gji/ggw193.

- 714 Sanders, C.O., Kanamori, H., 1984. A seismotectonic analysis of the anza seismic
715 gap, san jacinto fault zone, southern california. *J. Geophys. Res.: Solid Earth*
716 89, 5873–5890.
- 717 Sato, H., Fehler, M.C., Maeda, T., 2012. Seismic wave propagation and scattering
718 in the heterogeneous earth. volume 496. Springer.
- 719 Schwarz, B., 2019. An introduction to seismic diffraction, in: *Advances in Geo-*
720 *physics*. Elsevier. volume 60, pp. 1–64.
- 721 Schwarz, B., Krawczyk, C.M., 2020. Coherent diffraction imaging for enhanced
722 fault and fracture network characterization. *Solid Earth* 11, 1891–1907.
- 723 Shapiro, N.M., Campillo, M., 2004. Emergence of broadband rayleigh waves
724 from correlations of the ambient seismic noise. *Geophys. Res. Let.* 31.
- 725 Shapiro, S., Kneib, G., 1993. Seismic attenuation by scattering: theory and nu-
726 merical results. *Geophys. J. Int* 114, 373–391.
- 727 Share, P.E., Tábořík, P., Štěpančíková, P., Stemberk, J., Rockwell, T.K., Wade, A.,
728 Arrowsmith, J.R., Donnellan, A., Vernon, F.L., Ben-Zion, Y., 2020. Character-
729 izing the uppermost 100 m structure of the san jacinto fault zone southeast of
730 anza, california, through joint analysis of geological, topographic, seismic and
731 resistivity data. *Geophys. J. Int* 222, 781–794.
- 732 Sharp, R.V., 1967. San jacinto fault zone in the peninsular ranges of southern
733 california. *Geological Society of America Bulletin* 78, 705–730.
- 734 Touma, R., Blondel, T., Derode, A., Campillo, M., Aubry, A., 2021. A distortion
735 matrix framework for high-resolution passive seismic 3-d imaging: application

- 736 to the san jacinto fault zone, california. *Geophysical Journal International* 226,
737 780–794.
- 738 Wade, A.M., 2018. Geologic and structural characterization of shallow seismic
739 properties along the san jacinto fault at sage brush flat, southern california.
740 Master Thesis , 8.
- 741 Wapenaar, K., Draganov, D., Snieder, R., Campman, X., Verdel, A., 2010. Tuto-
742 rial on seismic interferometry: Part 1—basic principles and applications. *Geo-*
743 *physics* 75, 75A195–75A209.
- 744 Wesnousky, S.G., 1988. Seismological and structural evolution of strike-slip
745 faults. *Nature* 335, 340–343.
- 746 Xu, S., Ben-Zion, Y., Ampuero, J.P., 2012. Properties of inelastic yielding zones
747 generated by in-plane dynamic ruptures—ii. detailed parameter-space study.
748 *Geophys. J. Int* 191, 1343–1360.